Mott variable range hopping and bad-metal in lightly doped spin-orbit Mott insulator $BaIrO_3$

H. J. Harsan Ma,[1,2,*] P. Yang,[3] Z. S. Lim,[4,5] and Ariando[4,5,6]

[1]*Low Dimensional Quantum Physics & Device Group, State Key Discipline Laboratory of Wide Band Gap Semiconductor Technology, School of Microelectronics, Xidian University, 2 South Taibai Road, Xi'an 710071, China*

[2]*Physikalisches Institut and Center for Quantum Science (CQ) in LISA+, Universität Tübingen, Auf der Morgenstelle 14, D-72076 Tübingen, Germany*

[3]*Singapore Synchrotron Light Source (SSLS), National University of Singapore, 5 Research Link, 117603 Singapore*

[4]*NUSNNI-Nanocore, National University of Singapore, 117411 Singapore*

[5]*Department of Physics, National University of Singapore, 117542 Singapore*

[6]*NUS Graduate School for Integrative Sciences and Engineering, National University of Singapore, 117456 Singapore*

(Received 6 April 2017; revised manuscript received 30 April 2018; published 27 June 2018)

The Mott transition and the vicinity of a Mott insulating phase have constantly been a fertile ground for exploring exotic quantum states, most notably the high-T_c cuprates. The layered iridate represents another intriguing example. The nature of the Mott insulator phase and transition mechanism to a metallic state is still under debate. Much of the challenge originates from a series of energy scales involved in the electronics phases. Here, we report synthetization, characterization, and transport measurements on doped and undoped $Ba_{1-x}La_xIrO_3$ films grown on $SrTiO_3$. The films are fully strained up to 70 nm thick and have a tetragonal lattice structure. For a doping level of $x = 0.1$, a bad-metal state with linear temperature dependence of the resistivity beyond the Mott-Ioffe-Regel limit emerges in a wide temperature range down to a critical temperature $T_c \sim 30$ K, below which the system shows Mott variable range hopping (Mott VRH) conduction behavior. The ground state is confirmed to be insulating by the Mobius criterion. A strong correlation between the bad-metal state and Mott VRH localized state is found as the slope of the linear resistivity is inversely proportional to film thickness and the size of the Mott VRH activation energy Δ is linearly proportional to T_c. We further show that upon doping the spin-orbit Mott insulator, itinerant metallic regions coexist with localized regions within a nanoscale phase-separated ground state with a small activation energy. Our results shed light on the nature of the metallic state and a crossover to a bad-metal phase for doping the spin-orbit Mott insulator.

DOI: 10.1103/PhysRevMaterials.2.065003

I. INTRODUCTION

Iridate oxides have recently attracted intensive attention due to the emergence of novel electronic states associated with its large spin-orbit coupling (SOC). The spin-orbit coupling in iridates is about five to ten times stronger than that in the 3*d* transition-metal oxides. Despite the reduced on-site Coulomb repulsion strength in iridates due to the extension of the states, the ground states of many iridates such as Sr_2IrO_4 and Ba_2IrO_4 are found to be insulating, forming spin-orbit-driven Mott-gap states [1–6]. Although the electronic correlation energy is relatively small in these iridate oxides, SOC amplifies the effect of electronic correlation through narrowing the bandwidth of the conduction band. As a result, the Mott insulating ground state prevails in the perovskite iridate, such as $CaIrO_3$ [7] and $BaIrO_3$ [8,9], in contrast to ferromagnetic metallic $SrIrO_3$ [10]. The Mott insulator phase in iridates could arise due to the long-range or short-range antiferromagnetic order [4,5,7]. Semimetal and metallic phases emerge as the Mott insulator state is suppressed, and the electronic phase diagram displays similarities to that of the cuprates [6,9–11].

The perovskite iridate $BaIrO_3$ is markedly different from the canonical, band-driven itinerant picture. Its electrical resistivity was found to be nonmetallic with a gap of about 25–50 meV [11–13], which is very close to the edge of the Mott transition. By applying very large mechanical pressure, it is possible to make the ground state of $BaIrO_3$ insulating [14,15] or metallic [16] with a different structure. $BaIrO_3$ is monoclinic at ambient condition, with the space group $C2/m$, rather than the rhombohedral structure [11]. It was reported that $BaIrO_3$ could have a distorted hexagonal structure by high-pressure sintering, which instead leads to interesting electronic properties [15]. Spin-orbit Mott states [8] and charge ordering [9,13] predicted in $BaIrO_3$ within a Hubbard model is of great interest. Hence, investigations of $BaIrO_3$ have been thought to be a promising way to tune the physical properties of iridate compounds in order to ultimately reveal the theoretically predicted properties in the barium iridates and search for new electronic states [3,17–22] expanded from the original Mott state. However, synthesizing tetragonal $BaIrO_3$ crystals is a formidable task due to the fact that it requires a sophisticated combined high-pressure ($P \sim 25$ GPa) and high-temperature ($T \sim 1150\,^{\circ}$C) synthesis technique [23]. Experimental studies on $BaIrO_3$ have been limited to polycrystals or tiny single-crystal samples so far. Thus, there is a demand for large-area single-crystal and thin-film samples for the wide range of experimental

*Author to whom correspondence should be addressed: mahj07@xidian.edu.cn, harsanmhj@gmail.com

studies and the potential microelectronic device applications anticipated from this material.

II. EXPERIMENTS AND DISCUSSIONS

Here, we report the successful growth of tetragonal $Ba_{1-x}La_xIrO_3$ (BLIO) films on $SrTiO_3$(001) substrate and the observation of an intermediate bad-metal state with exact linear temperature-dependent resistivity and a bad-metal to Mott variable range hopping (Mott VRH) localized states transition in fully strained tetragonal $Ba_{1-x}La_xIrO_3$. The ground state of all the samples is always insulating, which is confirmed by the Mobius criterion. The metallic sample (at the intermediate- and high-temperature ranges) shows coexisting itinerant metallic regions and localized regions at nanoscale with a suppression of the original gap in the ground state down to an activation energy of a few meV. This bad-metal state bears similarities with well-studied strongly correlated systems such as doped Sr_2IrO_4 and underdoped cuprates and emerges from a suppression of the original gap via doping in a nonmetallic ground state.

$Ba_{1-x}La_xIrO_3$ ($x = 0$ and 0.1) thin films were grown by pulsed laser deposition methods. La^{3+} substitution for Ba^{2+} [24,25] is proven suitable to dope electrons into perovskites with minimal disorder-induced scattering of in-plane carriers compared to other ions such as Sr^{2+} and Ca^{2+} [26]. Moreover, substitution of Ba by La also preserves the structure of undoped $BaIrO_3$ and the ionic environment of Ir, as Ba and La has a comparable atomic size. Polycrystalline $Ba_{1-x}La_xIrO_3$ ($x = 0$, 0.1) targets were used for the depositions. A $Ba_{1-x}La_xIrO_3$ solid solution was prepared by a conventional solid-state route. A stoichiometric amount of analytical reagent grade BaO ($\geqslant$99.9%), La_2O_3 ($\geqslant$99.9%), and IrO_2 ($\geqslant$99.9%) was mixed with acetone for 1 h by ball milling. The mixed powder was then calcined in a furnace at 900 °C for 24 h. This calcined powder was pressured to form the target using a cylindrical die (12 mm diameter) and jack press. The target pellets were sintered at 1000 °C for 12 h. Epitaxial $Ba_{1-x}La_xIrO_3$ ($x = 0$,0.1) films were then grown on a TiO_2-terminated (001)-orientated $SrTiO_3$ single-crystal substrate in a pulsed laser deposition system using a KrF excimer laser with a wavelength of 248 nm, pulse width of approximately 15 ns, and system base pressure of 5×10^{-8} Torr. The laser energy density was maintained at 1.6 J/cm^2 with a pulse frequency of 2 Hz for all the depositions. The temperature of the samples was controlled by a thermal radiation heater and was 612 °C. The chamber pressure was fixed at 50 mTorr for the whole deposition process. After growth, the samples were cooled to room temperature in a ramping rate of 15 °C per minute.

The ambient-phase structure of $BaIrO_3$ is monoclinic with a space group of $C2/m$. There are a total of four Ir_3O_{12} trimers per primitive unit cell, whose experimental parameters are $a = 10.0052$ Å, $b = 5.7514$ Å, $c = 15.1742$ Å, and $\beta = 103.274°$ [11,13,14]. The lattice mismatch between a bulk $BaIrO_3$ and $SrTiO_3$ is 44%, resulting in a large in-plane compressive strain on the $BaIrO_3$ thin film. Using the Young's modulus of $BaIrO_3$ of about 215 GPa, the in-plane pressure of approximately 94 GPa would be exerted on the $BaIrO_3$ films by the compressive strain, which satisfies the high-pressure conditions required for the synthesis of a bulk tetragonal $BaIrO_3$ [23,27].

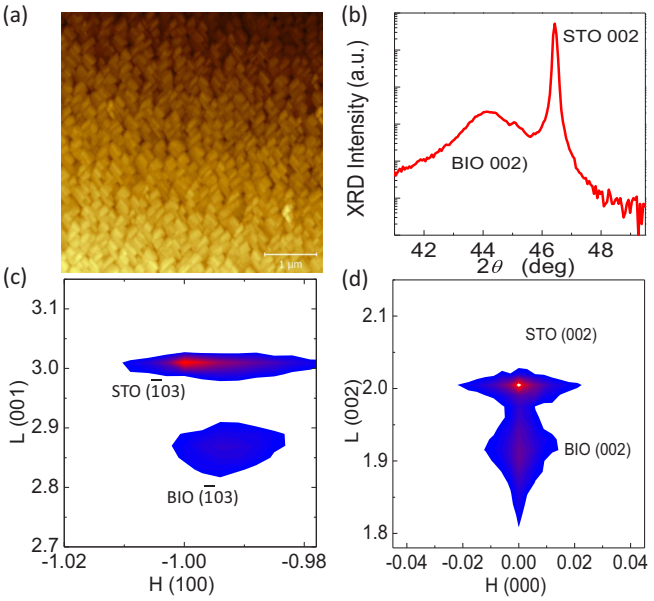

FIG. 1. Structure characterization of BLIO film on $SrTiO_3$(001) substrate. (a) Atomic force microscopy images of 41 nm BLIO sample. (b) A θ-2θ scan where the $Ba_{1-x}La_xIrO_3$ 002 peaks are clearly labeled. (c),(d) X-ray reciprocal-space map (RSM) near STO ($\bar{1}03$) and (002), respectively.

The structural properties of the epitaxial $Ba_{1-x}La_xIrO_3$ thin films were characterized with x-ray diffractometry. The lattice parameters were determined for a 70-nm-thick $Ba_{1-x}La_xIrO_3$ ($x = 0.1$) film using reciprocal space vectors (RSVs) [28]. The RSV method uses three reciprocal lattice vectors to determine the lattice parameters and crystal system of epitaxial thin films. The lattice parameters of single-crystal substrates are employed as references to correct the systematic experimental errors of RSVs of thin films. The correction of RSVs, derivation of raw unit cell, and subsequent conversion to the Niggli unit cell and the Bravais unit cell could be determined by matrix calculation with two different methods in three-dimensional (3D) reciprocal space and 6D G^6-space, respectively. One could refer to Ref. [28] for details. X-ray reciprocal space mapping (RSM) was also performed for (002), ($\bar{1}03$), and (103) in hkl space to reveal the strain status in the film. Figure 1(a) shows an atomic force microscopy (AFM) image of the film and Fig. 1(b) shows a θ-2θ scan with 002 peak of the film. RSM near $SrTiO_3$ ($\bar{1}03$) [Fig. 1(c)] shows that the film is fully strained. We found that the film has a fully strained tetragonal structure up to 70 nm. RSM near the $SrTiO_3$ (002) [Fig. 1(d)] shows that the normal of the film was grown exactly parallel to that of the substrate. The lattice parameters of the film calculated from the RSMs are $a = 3.911$ Å and $c = 4.086$ Å. An x-ray $2\theta/\omega$ scan showed no sign of complex periodic structures such as Ba_2IrO_4 or $Ba_3Ir_2O_7$. The x-ray RSM and rocking curve show that the film has a good crystalline quality.

A transport resistivity measurement was done using a commercial PPMS of Quantum Design. $BaIrO_3$ films showed semiconducting behavior with a very tiny band gap below 10 meV, which could be obtained by fitting the semiconducting resistivity as a function of temperature, $\rho_{XX}(T) = \rho_0 \exp(E_g/2K_BT)$,

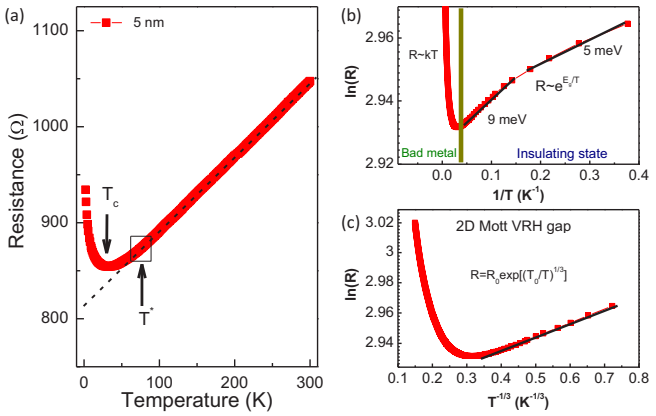

FIG. 2. (a) Electrical resistance of 5-nm-thick $Ba_{1-x}La_xIrO_3$ ($x = 0.1$) film as a function of temperature. The dashed black line is a linear fit to the data between 100 and 300 K. Below a temperature T^*, $R(T)$ deviates from its linear-T behavior and develops a pronounced upturn at low temperature. (b) $\ln(R)$ as a function of $1/T$ showing the Mott VRH activation energy. (c) $\ln(R)$ as a function of $1/T^{1/3}$ indicating the 2D Mott-VRH below T_c.

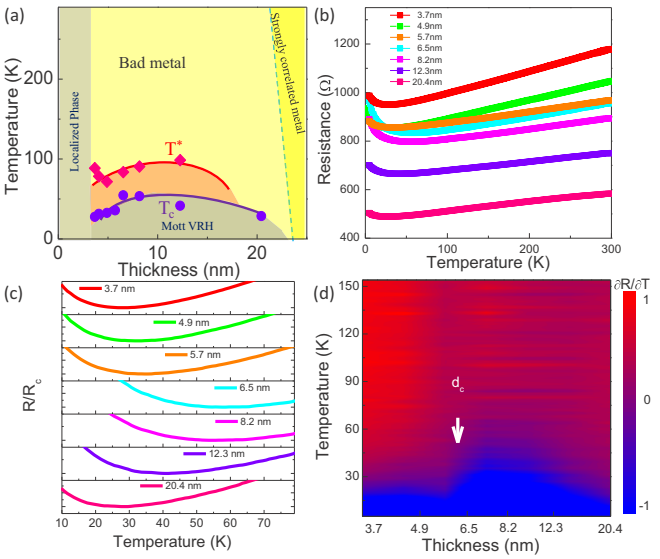

FIG. 3. Bad-metal to Mott VRH localized state transition in BLIO films with various thickness. (a) Temperature-thickness phase diagram of BLIO. Filled violet circles represent the MIT critical temperature T_c, and filled pink oblique squares represent T^* as shown in Fig. 2. (b) Temperature dependence of resistance $R(T)$ as a function of film thickness d. (c) Close-up view of the metal-insulator transition temperature T_c as a function of d. The data shows that $d_c \sim 6.5$ nm is a crossover thickness. (d) Temperature derivative of resistance $k \equiv \partial R/\partial T$ as a function of d at temperatures near the crossover points. The white arrow shows the position of the crossover point at $(d = d_c, T = T_c)$.

yielding $E_g < 10-20$ meV (see Fig. S1 in the Supplemental Material [29]). Intriguingly, the $Ba_{1-x}La_xIrO_3$ ($x = 0.1$) film grown on a $SrTiO_3(001)$ substrate shows metallic behavior [Fig. 2(a)] under very rigorous growth conditions, as mentioned previously. We demonstrate here that the observed metallic state is a bad-metal state above T_c, defined as the minimum of the resistivity in Fig. 2(a). The mobility of the samples $\sim 1\,\mathrm{cm^2\,V^{-1}\,s^{-1}}$ (see Fig. S2(b) in the Supplemental Material [29]) is very close to the Mott-Ioffe-Regel (MIR) limit $\mu_{\mathrm{MIR}} = ea/\hbar(3\pi^2 n)^{1/3} \sim 1.2\,\mathrm{cm^2\,V^{-1}\,s^{-1}}$, while the resistivity is not saturating at the MIR limit of $\rho_{\mathrm{MIR}} = 3\pi^2\hbar/e^2k_F^2a \sim 1000\,\mu\Omega$cm but goes beyond this value up to $\sim 3000\,\mu\Omega$cm at 300 K. Furthermore, the metallic BLIO films [Fig. 2(a)] are found to exhibit an exact linear temperature-dependent resistivity from above 300 K to T^*. Below $T_c = 30$ K, the samples show a resistivity upturn [Fig. 2(b)], which could be fitted well by the 2D Mott VRH model [Fig. 2(c)]. The extracted Mott VRH activation energy is about a few meV to $\sim 10-20$ meV, showing a suppression of the gap in $BaIrO_3$ [11–13]. This means that the ground state of the $Ba_{1-x}La_xIrO_3$ ($x = 0.1$) films is still a nonmetallic state. The Mott VRH activation energy of undoped $BaIrO_3$ film ($x = 0$) is also suppressed to about 4–5 meV to 11 meV close to doped films, though undoped films have high resistivity (see Fig. S1 of the Supplemental Material [29]). In the ultrathin samples, the Mott VRH activation energy of the undoped films is smaller than the doped films. A possible mechanism is that the band gap can increase with n doping due to the Burstein-Moss effect. Basically the electrons from the donors "fill up" the density of states near the conduction-band minimum, effectively raising the band gap. Alternatively, the localized areas could possibly have a different structure with a different gap energy, coexisting with electronic phase separation.

The phase diagram of BLIO films on $SrTiO_3$ substrate as a function of film thickness and temperature, shown in Fig. 3(a), clearly shows that there is a bad-metal to insulating ground-state metal-insulator transition (MIT). Figure 3(b) shows the temperature dependence of resistance $R(T)$ of BLIO samples with different thickness d. The samples are metallic at high temperatures for thicknesses larger than 3.3 nm and are semiconducting below 3.3 nm. The $R(T)$ graphs show a critical temperature T_c where the MIT occurs, below which the resistance starts to increase. The $R(T)$ is also continuous at T_c, corresponding to the second-order MIT [21]. Although the resistance of the samples at high temperature decreases when the thickness increases, the T_c is not a monotonic function of thickness [Fig. 3(c)]. One could see that there is a crossover thickness d_c about 6.5 nm at which T_c and the temperature derivative of resistance, $k \equiv \partial R/\partial T$, show extremum [Fig. 3(d)]. These results show that there is a crossover thickness for MIT in the BLIO/$SrTiO_3$ system. Normally, a bad-metal undergoes a crossover to either a Fermi-liquid or a non-Fermi-liquid ground state at very low temperatures. In the BLIO system, the sample goes to a localized state instead.

This has been studied in many systems that possess a linear temperature (T)-dependent resistivity (ρ) regardless of their unclear microscopic origins [30,31]. The $\rho \sim T$ relation could be explained quantitatively by the Bloch-Grüneisen formula in the case of electron-phonon scattering produced by linear-T resistivity [31]. In 2D systems, surface phonon softening could further lead to a reduced Debye temperature and thus the $\rho \sim T$ relation observed at a wider temperature range [30]. The slope of the linear T-dependent resistivity k is the scaling parameter depending on the material and the

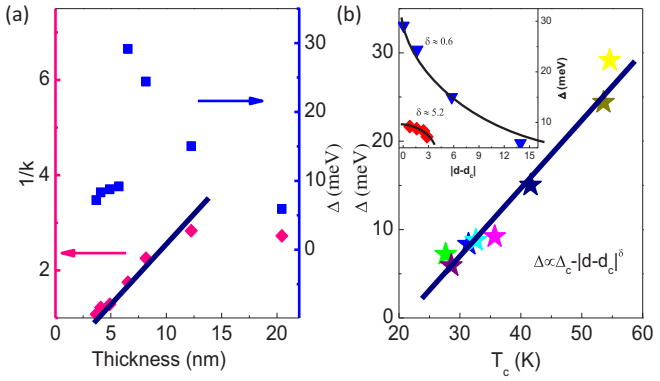

FIG. 4. Suppression of the activation energy in BLIO as a function of film thickness and the correlation between the Mott VRH localized states and bad-metal states. (a) $1/k$ (left) of the bad-metal states and Mott VRH activation energy Δ (right) as a function of thickness d. (b) Δ as a function of T_c for different thickness showing a linear dependence. Inset: Plot of Δ as a function of $|d - d_c|$ showing different scaling behavior for $d < d_c$ and $d > d_c$. The dark solid lines are fitting to the scaling equation $\Delta = \Delta_c - |d - d_c|^{\delta}$, where δ is the scaling parameter.

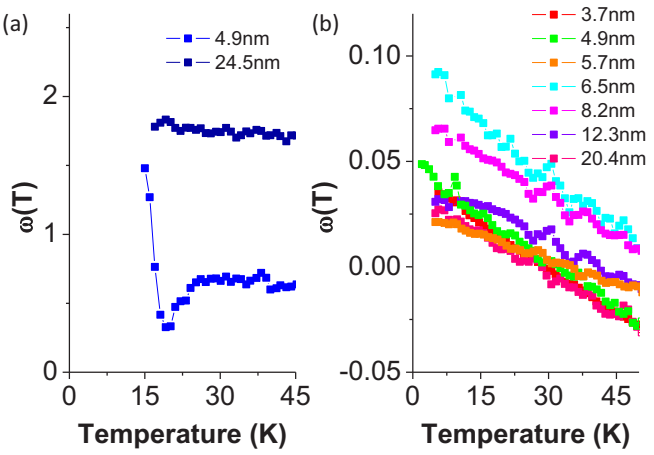

FIG. 5. Mobius criterion $\omega(T) = d \ln \sigma(T)/d \ln T$ of the insulating ground states in both (a) undoped ($x = 0$) and (b) doped ($x = 0.1$) $Ba_{1-x}La_xIrO_3$ films. The undoped $BaIrO_3$ ($x = 0$) films show either a finite value (for thickness of 24.5 nm) or a diverging value (for thickness of 4.9 nm) of $w(T)$ as $T \to 0$, indicating that the samples are insulator. The doped $BaIrO_3$ ($x = 0.1$) films show finite values (for all samples) of $w(T)$ as $T \to 0$, indicating that the samples are also genuine insulators at low temperatures.

Debye temperature. One question that is always of interest is whether the T-linear resistivity can be associated with an $\hbar/(k_B T)$ time scale [32,33]. It has been shown that the dc resistivity $\rho_{dc} = 1/\sigma_{dc} \sim m/ne^2 \cdot k_B T/\hbar$ [32]. Assuming a single Fermi surface and electron-type carrier and taking into account our results shown in Figs. 3(d), 4(a), and S2 (see Supplemental Material [29]), we could deduce an effective mass of $\sim 10 m_e$. In the spirit of Ref. [33], by introducing the 2D isotropic-relaxation-time approximation, we could calculate the scattering rate by plotting $ne^2/(k_B k_F) d\rho/dT$ as a function of $1/v_F$. Thus, $ne^2/(k_B k_F) d\rho/dT$ is 0.41×10^{-5} (m/s)$^{-1}$. By using the result in Fig. 2 of Ref. [33], the Fermi velocity v_F is about 2.4×10^5 m/s. This indicates the linear-T resistivity in very different systems and microscopic origins obeying similar scattering rates captured by the same mathematic model as demonstrated recently in Ref. [32]. Correspondingly, the scattering rate $1/\tau = ne^2 v_F \rho/(\hbar k_F)$ is 1.3×10^{14} s^{-1}, which corresponds to a scattering time of 7.7 fs. The Planckian time scale $k_B T/\hbar \sim 25$ fs is much larger than the scattering time we obtained here. We further consider the $\rho = \rho_0 + d\rho/dT$ and $1/\tau = 1/\tau_0 + 1/\tau_s$ where $1/\tau_0$ is T independent and $1/\tau_s$ is the scattering which leads to T-linear resistivity; then we extract a value of $1/\tau_s = ne^2 v_F d\rho/dT^* T/(\hbar k_F)$ leading to a scattering time of 18.4 fs which is of the order of the Planckian time scale.

We plot $1/k$ of the linear T-dependent resistivity in the bad-metal states as well as the extracted activation energy Δ in the localized states as a function of film thickness in Fig. 4(a). Surprisingly, we find $1/k$ is linearly proportional to the film thickness d relation for all the films under 20 nm, while the activation energy abruptly changes at d_c similar to the behavior of T_c, as shown in Fig. 3(a). Thus we plot the activation energy Δ as a function of T_c in Fig. 4(b), which surprisingly shows a linear dependence. This indicates that there is a strong correlation between the formation of the localized states and the bad-metal states crossing the critical MIT temperature T_c. We further demonstrate that the scaling behaviors of Δ vs $|d - d_c|$ are different for branches below and above critical thickness d_c [inset of Fig. 4(b)], indicating a thermodynamics driving force of the MIT. This instead fits well with the theory of hydrodynamics of short-range quantum critical fluctuations of incommensurate density induced bad-metals even without strong disorder [33]. The size of the activation energy surprisingly approaches to a vanishing size of about a few meV, making the system very promising for further engineering Dirac metal and searching for the possible superconducting phase. The linear dependence of $\Delta \sim Tc$ means the temperature is the only energy scale which determines the occurrence of the Mott VRH localized states.

It is well known that many doped oxide materials show a resistivity upturn at low temperatures, but which may not be due to an insulating ground state. There is a strict criterion to determine whether the low-temperature resistivity is that of a genuine metal or an insulator, given by Mobius [34–36]. The Mobius criterion requires one to plot the function $\omega(T) = d \ln \sigma(T)/d \ln(T)$ vs T or $\omega(T) = d \ln \sigma(T)/d \ln(T)$ vs $T^{1/2}$. As has been shown by Mobius *et al.*, the dependence of $\omega(T)$ vs T is far more sensitive for determining the transition than ρ vs T. $\omega(T) \to 0$ implies a metallic character of the conduction, whereas a diverging or finite value for $\omega(T)$ as $T \to 0$ indicates that the sample is an insulator. The analysis shown in Fig. 5 shows that both undoped and doped samples have either a finite value or a diverging value as $T \to 0$. This indicates that undoped samples are genuine insulators [Fig. 5(a)] and doped samples also have an insulating ground state but quite close to the metallic border [Fig. 5(b)]. Thus the resistance upturns below T_c are due to the metal-insulator transition for doped samples.

In order to have a better understanding of the formation of the MIT and metallic phase in the insulating ground state, scan-

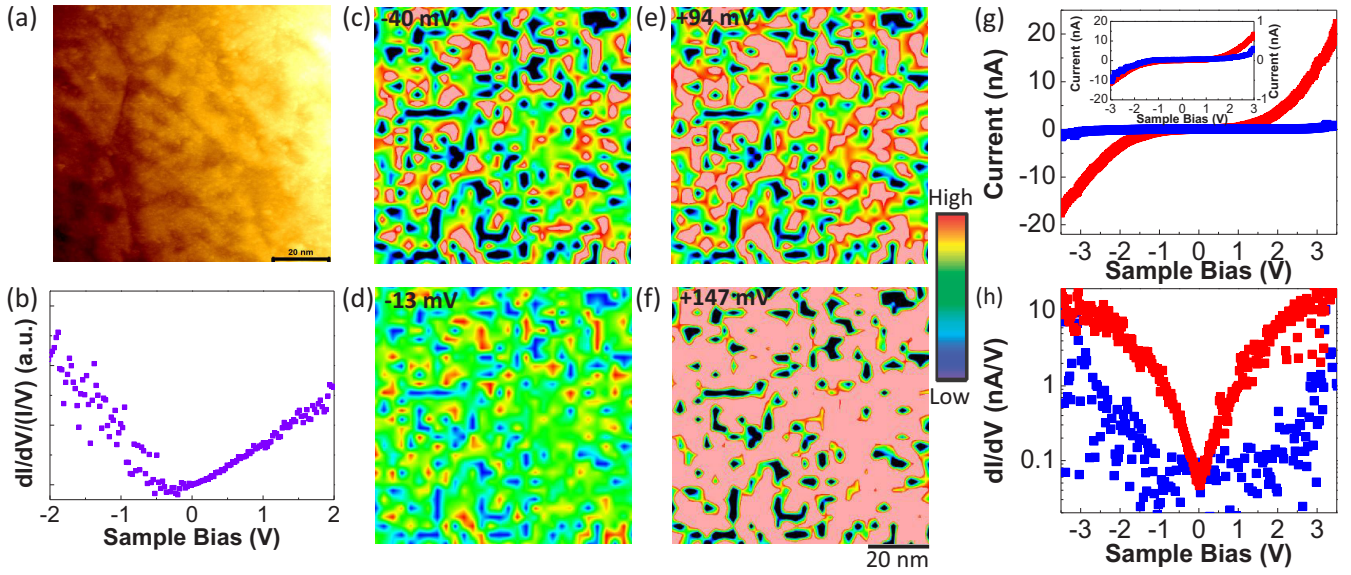

FIG. 6. Scanning tunneling microscopy/spectroscopy of 5 nm film sample at 300 K. (a) Topography of the sample which has a roughness of ∼0.3 nm. The size of the imaged sample area is around 96 × 96 nm^2. (b) Density of state (DOS) averaged $dI/dV/(I/V)$ vs V curve showing that the density of state linearly changes with bias voltage with different slopes for positive and negative voltages. (c)–(f) $dI/dV/(I/V)$ mapping with voltage bias at −40, −13, 94, and 147 mV, respectively. The spectra show the coexistence of localized and itinerant regions. (g),(h) IV and dI/dV vs sample bias for two blue (dark) (localized) and red (bright) (itinerant) regions in (c)–(f) indicated by the white cross. Inset in (g) shows IV curve with a different scale, showing a similar gap behavior.

ning tunneling microscopy/spectroscopy (STM/STS) measurements were performed on a sample with thickness of 5 nm at 290 K. Figure 6 shows the resulting topography of STS measurements exploring the local density of states (LDOS) [Figs. 6(c)–6(f)]. Strong inhomogeneity across nanometer length scales in the sample is apparent and reveals the coexistence of two distinct local environments. The blue (dark) regions with low LDOS in the corresponding map reveal localized regions [blue dotted line in Figs. 6(g) and 6(h)], while the red (bright) regions reveal itinerant metallic regions with an enhanced LDOS [red dotted line in Figs. 6(g) and 6(h)], consistent with recent studies [37]. The striking nanoscale coexistence of localized regions and itinerant metallic regions in this sample demonstrates that the sample segregates into electronically distinct regions. In Fig. 6(g), the IV curves of the metallic region and localized region behave differently in the same scale; however, we surprisingly find that the general IV behavior of the two regions is similar. The main difference is the magnitude of the conductance (or tunneling current). In the metallic region, the conductance starts to increase much faster at about $+/-1$ V [Fig. 6(h)], while in the localized region, the conductance starts to increase rapidly at about $+2/-1$ V. Since the on-site Coulomb energy of $BaIrO_3$ is in the range between 2.0 and 3.0 eV [8], the position of the conduction band and valence band [lower Hubbard band (LHB) and the upper Hubbard band (UHB) in the Mott insulator] could be detected in the measurements. The LHB and UHB are still visible in the case of slight doping, though there could be some shifting and modifications. Though the conductance behavior is different in the metallic regions and localized regions, we observe a large gap in the magnitude of about 2–3 V in both regions. At ultrathin films below 3 nm [see Fig. 3(a)], the samples are nonmetallic at the whole measured temperature range below 400 K, which could be due to Anderson localization [38]. The thickness-dependent scaling behavior [Figs. 3(a) and 3(b) and the inset of Fig. 4(b)] could thus be understood in the content of thermodynamics as a percolative metal-insulator transition [39], along with the appearance of a crossover thickness d_c [40]. The percolation thermodynamics drives the correlated bad-metal and Mott VRH localized state MIT transition. A DOS mapping as a function of bias voltage and q vector (see Fig. S3 of the Supplemental Material [29]) could be extracted from STS mapping, as shown in Fig. 6. Figure S3(b) (see Supplemental Material [29]) is the line profiles of Fig. S3(a) for certain bias voltages showing a fluctuating density wave, which further supports the hydrodynamics theory [33,41].

We note that the samples surprisingly show electron-hole asymmetry, as shown in Fig. 6(b) [42]. What is notable is the nearly linear dispersion appearing at the Fermi level for the conduction band ($V > 0$), while it is different for the valence band ($V < 0$) [Fig. 7(b)]. The conduction band and valence band extrapolate to a point around −0.2 eV and continue to disperse quasilinearly at higher energy. This hints at the exotic bad-metal states observed in lightly doped $BaIrO_3$ films in contrast to conventional states [43,44]. In cuprates, a linear T-dependent R in the so-called pseudogap phase with strikingly similar phenomenology is often associated with superconductivity [45] or competing ordered states between superconductivity and charge density wave [46,47]. Yet, the bad-metal states in the BLIO samples persist up to about 100 K, while the samples show no superconductivity down to 2 K. This rather makes us think of pseudogaplike phases and even possibly a superconducting state in layered iridates not only limited to high-T_c cuprates such as a 214 structure [48], but rather to extend it to a 113 or other structures.

III. SUMMARY

The existence of a vanishing meV-level activation energy of Mott VRH localized states and linear T-dependent R above the MIR limit in a doped iridate, and the correlation between the metallic states and the insulating ground states, strongly supports the bad-metal nature of the doped iridate. Furthermore, the appearance of localized regions in the globally gapless sample makes the bad-metal state more extraordinary as compared to the conventional chemically doped metallic states in semiconductor samples. An important issue that immediately arises is whether the bad-metal states appear due to magnetic order or correlation effect [37,38,44]. Theoretically, it was pointed out that unconventional states such as topological states and exotic superconducting pairing symmetry could be realized in doped spin-orbit Mott insulators [18,49]. It deserves further investigations to explore the distinct signatures of predicted unconventional states in doped spin-orbit Mott insulators.

ACKNOWLEDGMENTS

We acknowledge A. Rana for help with the measurements. We wish to thank X. R. Wang and J. Guo for useful discussions. We thank the Singapore National Research Foundation (NRF) under the Competitive Research Programs (CRP Award No. NRF-CRP15-2015-01) and the NUS FRC (AcRF Tier 1 Grant No. R-144-000-364-112). P.Y. is supported by SSLS via NUS Core Support, Grant No. C-380-003-003-001. The authors would also like to acknowledge the Singapore Synchrotron Light Source (SSLS) for providing the facility necessary for conducting the research. The Laboratory is a National Research Infrastructure under the National Research Foundation (NRF) Singapore. H.J.HM is partially supported by the Teach@Tübingen program and a Humboldt fellowship. We also acknowledge financial support from XiDian University.

[1] B. J. Kim, Hosub Jin, S. J. Moon, J.-Y. Kim, B.-G. Park, C. S. Leem, Jaejun Yu, T. W. Noh, C. Kim, S.-J. Oh, J.-H. Park, V. Durairaj, G. Cao, and E. Rotenberg, Novel $J = 1/2$ Mott State Induced by Relativistic Spin-Orbit Coupling in Sr_2IrO_4, Phys. Rev. Lett. **101**, 076402 (2008).

[2] B. J. Kim, H. Ohsumi, T. Komesu, S. Sakai, T. Morita, H. Takagi, and T. Arima, Phase-sensitive observation of a spin-orbital Mott state in Sr_2IrO_4, Science **323**, 1329 (2009).

[3] G. Jackeli and G. Khaliullin, Mott Insulators in the Strong Spin-Orbit Coupling Limit: From Heisenberg to a Quantum Compass and Kitaev Models, Phys. Rev. Lett. **102**, 017205 (2009).

[4] H. Okabe, M. Isobe, E. Takayama-Muromachi, A. Koda, S. Takeshita, M. Hiraishi, M. Miyazaki, R. Kadono, Y. Miyake, and J. Akimitsu, Ba_2IrO_4: A spin-orbit Mott insulating quasi-two-dimensional antiferromagnet, Phys. Rev. B **83**, 155118 (2011).

[5] S. Boseggia, R. Springell, H. C. Walker, H. M. Rønnow, C. Rüegg, H. Okabe, M. Isobe, R. S. Perry, S. P. Collins, and D. F. McMorrow, Robustness of Basal-Plane Antiferromagnetic Order and the $J = 1/2$ State in Single-Layer Iridate Spin-Orbit Mott Insulators, Phys. Rev. Lett. **110**, 117207 (2013).

[6] J.-M. Carter, V. V. Shankar, M. A. Zeb, and H.-Y. Kee, Semimetal and topological insulator in perovskite iridates, Phys. Rev. B **85**, 115105 (2012).

[7] M. Moretti Sala, K. Ohgushi, A. Al-Zein, Y. Hirata, G. Monaco, and M. Krisch, $CaIrO_3$: A Spin-Orbit Mott Insulator Beyond the $j_{\text{eff}} = 1/2$ Ground State, Phys. Rev. Lett. **112**, 176402 (2014).

[8] W.W. Ju, G.-Q. Liu, and Z. Q. Yang, Exotic spin-orbital Mott insulating states in $BaIrO_3$, Phys. Rev. B **87**, 075112 (2013).

[9] G. Cao, J. E. Crow, R. P. Guertin, P. F. Henning, C. C. Homes, M. Strongin, D. N. Basov, and E. Lochner, Charge density wave formation accompanying ferromagnetic ordering in quasi-one-dimensional $BaIrO_3$, Solid State Commun. **113**, 657 (2000).

[10] G. Cao, V. Durairaj, S. Chikara, L. E. DeLong, S. Parkin, and P. Schlottmann, Non-Fermi-liquid behavior in nearly ferromagnetic $SrIrO_3$ single crystals, Phys. Rev. B **76**, 100402(R) (2007).

[11] K. Maiti, R. S. Singh, V. R. R. Medicherla, S. Rayaprol, and E. V. Sampathkumaran, Origin of Charge Density Wave Formation in Insulators from a High Resolution Photoemission Study of $BaIrO_3$, Phys. Rev. Lett. **95**, 016404 (2005).

[12] G. Cao, X. N. Lin, S. Chikara, V. Durairaj, and E. Elhami, High-temperature weak ferromagnetism on the verge of a metallic state: Impact of dilute Sr doping on $BaIrO_3$, Phys. Rev. B **69**, 174418 (2004).

[13] I. Terasaki, S. Ito, T. Igarashi, S. Asai, H. Taniguchi, R. Okazaki, Y. Yasui, K. Kobayashi, R. Kumai, H. Nakao, and Y. Murakami, Novel Charge Ordering in the Trimer Iridium Oxide $BaIrO_3$, Crystals **6**, 27 (2016).

[14] O. B. Korneta, S. Chikara, S. Parkin, L. E. DeLong, P. Schlottmann, and G. Cao, Pressure-induced insulating state in $Ba_{1-x}R_xIrO_3$ (R = Gd, Eu) single crystals, Phys. Rev. B **81**, 045101 (2010).

[15] M. A. Laguna-Marco, G. Fabbris, N. M. Souza-Neto, S. Chikara, J. S. Schilling, G. Cao, and D. Haskel, Different response of transport and magnetic properties of $BaIrO_3$ to chemical and physical pressure, Phys. Rev. B **90**, 014419 (2014).

[16] J.-G. Cheng, T. Ishii, H. Kojitani, K. Matsubayashi, A. Matsuo, X. Li, Y. Shirako, J.-S. Zhou, J. B. Goodenough, C. Q. Jin, M. Akaogi, and Y. Uwatoko, High-pressure synthesis of the $BaIrO_3$ perovskite: A Pauli paramagnetic metal with a Fermi liquid ground state, Phys. Rev. B **88**, 205114 (2013).

[17] X. Wan, A. M. Turner, A. Vishwanath, and S. Y. Savrasov, Topological semimetal and Fermi-arc surface states in the electronic structure of pyrochlore iridates, Phys. Rev. B **83**, 205101 (2011).

[18] F. Wang and T. Senthil, Twisted Hubbard Model for Sr_2IrO_4: Magnetism and Possible High Temperature Superconductivity, Phys. Rev. Lett. **106**, 136402 (2011).

[19] D. Pesin and L. Balents, Mott physics and band topology in materials with strong spin-orbit interaction, Nat. Phys. **6**, 376 (2010).

[20] J.-M. Carter, V. V. Shankar, and H.-Y. Kee, Theory of magnetic structure in layered iridates: Spin-orbit band or Mott insulators, Phys. Rev. B **88**, 035111 (2013).

[21] C. L. Kane and E. J. Mele, Z_2 Topological Order and the Quantum Spin Hall Effect, Phys. Rev. Lett. **95**146802 (2005).

[22] N. A. Bogdanov, V. M. Katukuri, J. Romhányi, V. Yushankhai, V. Kataev, B. Büchner, J. van den Brink, and L. Hozoi, Orbital reconstruction in nonpolar tetravalent transition-metal oxide layers, Nat. Commun. **6**, 7306 (2015).

[23] J. G. Zhao, L. X. Yang, Y. Yu, F. Y. Li, R. C. Yu, and C. Q. Jin, Structural and physical properties of the 6M $BaIrO_3$: A new metallic iridate synthesized under high pressure, Inorg. Chem. **48**, 4290 (2009).

[24] M. Ge, T. F. Qi, O. B. Korneta, D. E. De Long, P. Schlottmann, W. P. Crummett, and G. Cao, Lattice-driven magnetoresistivity and metal-insulator transition in single-layered iridates, Phys. Rev. B **84**, 100402(R) (2011).

[25] A. de la Torre, S. McKeown Walker, F. Y. Bruno, S. Riccó, Z. Wang, I. Gutierrez Lezama, G. Scheerer, G. Giriat, D. Jaccard, C. Berthod, T. K. Kim, M. Hoesch, E. C. Hunter, R. S. Perry, A. Tamai, and F. Baumberger, Collapse of the Mott Gap and Emergence of a Nodal Liquid in Lightly Doped Sr_2IrO_4, Phys. Rev. Lett. **115**, 176402 (2015).

[26] K. M. Shen, N. Kikugawa, C. Bergemann, L. Balicas, F. Baumberger, W. Meevasana, N. J. C. Ingle, Y. Maeno, Z.-X. Shen, and A. P. Mackenzie, Evolution of the Fermi Surface and Quasiparticle Renormalization through a van Hove Singularity in $Sr_{2-y}La_yRuO_4$, Phys. Rev. Lett. **99**, 187001 (2007).

[27] X. Gao, S. Lee, J. Nichols, T. L. Meyer, T. Z. Ward, M. F. Chisholm, and H. N. Lee, Nanoscale self-templating for oxide epitaxy with large symmetry mismatch, Sci. Rep. **6**, 38168 (2016).

[28] P. Yang, H. J. Liu, Z. H. Chen, L. Chen, and J. Wang, Unit-cell determination of epitaxial thin films based on reciprocal-space vectors by high-resolution X-ray diffractometry, J. Appl. Cryst. **47**, 402 (2014).

[29] See Supplemental Material at http://link.aps.org/supplemental/10.1103/PhysRevMaterials.2.065003 for the fitting to a simple semiconductor and Mott VRH model, and carrier density extracted from Hall resistivity measurements.

[30] S. Kim, H. Suhl, and I. K. Schuller, Surface Phonon Scattering in the Electrical Resistivity on Co/Ni Superlattices, Phys. Rev. Lett. **78**, 322 (1997).

[31] O. Madelung, *Introduction to Solid-State Theory* (Springer-Verlag, Berlin, 1978), pp. 210–218.

[32] J. A. N. Bruin, H. Sakai, R. S. Perry, and A. P. Mackenzie, Similarity of scattering rates in metals showing T-linear resistivity, Science **339**, 804 (2013).

[33] L. V. Delacrétaz, B. Goutéraux, S. A. Hartnoll, and A. Karlsson, Bad metals from fluctuating density waves, SciPost Phys. **3**, 025 (2017).

[34] A. Mobius, Solid State Commun. **73**, 215 (1990).

[35] A. Möbius, C. Frenzel, R. Thielsch, R. Rosenbaum, C. J. Adkins, M. Schreiber, H.-D. Bauer, R. Grötzschel, V. Hoffmann, T. Krieg, N. Matz, H. Vinzelberg, and M. Witcomb, Metal-insulator transition in amorphous $Si_{1-x}Ni_x$: Evidence for Mott's minimum metallic conductivity, Phys. Rev. B **60**, 14209 (1999).

[36] K. P. Rajeev and A. K. Raychaudhuri, Quantum corrections to the conductivity in a perovskite oxide: A low-temperature study of $LaNi_{1-x}Co_xO_3$ ($0 \leqslant x \leqslant 0.75$), Phys. Rev. B **46**, 1309 (1992).

[37] C. Dhital *et al.*, Carrier localization and electronic phase separation in a doped spin-orbit-driven Mott phase in $Sr_3(Ir_{1-x}Ru_x)_2O_7$, Nat. Commun. **5**, 3377 (2013).

[38] E. Mikheev, A. J. Hauser, B. Himmetoglu, N. E. Moreno, A. Janotti, C. G. Van de Walle, and S. Stemmer, Tuning bad metal and non-Fermi liquid behavior in a Mott material: Rare-earth nickelate thin films, Sci. Adv. **1**, e1500797 (2015).

[39] J. Kokalj and R. H. McKenzie, Thermodynamics of a Bad Metal–Mott Insulator Transition in the Presence of Frustration, Phys. Rev. Lett. **110**, 206402 (2013).

[40] M. Mokhtari, L. Zekri, A. Kaiss, and N. Zekri, Effect of film thickness on the width of percolation threshold in metal-dielectric composites, Condens. Matter Phys. **19**, 43001 (2016).

[41] L.Chaix *et al.*, Dispersive charge density wave excitations in $Bi_2Sr_2CaCu_2O_{8C\delta}$, Nat. Phys. **13**, 952 (2017).

[42] K.-K. Bai, Y.-C. Wei, J.-B. Qiao, S.-Y. Li, L.-J. Yin, W. Yan, J.-C. Nie, and L. He, Detecting giant electron-hole asymmetry in a graphene monolayer generated by strain and charged-defect scattering via landau level spectroscopy, Phys. Rev. B **92**, 121405(R) (2015).

[43] M. Hashimoto, R.-H. He, K. Tanaka, J.-P. Testaud, W. Meevasana, R. G. Moore, D. Lu, H. Yao, Y. Yoshida, H. Eisaki, T. P. Devereaux, Z. Hussain, and Z.-X. Shen, Particle-hole symmetry breaking in the pseudogap state of Bi2201, Nat. Phys. **6**, 414 (2010).

[44] Y. J. Yan, M. Q. Ren, H. C. Xu, B. P. Xie, R. Tao, H. Y. Choi, N. Lee, Y. J. Choi, T. Zhang, and D. L. Feng, Electron-Doped Sr_2IrO_4: An Analogue of Hole-Doped Cuprate Superconductors Demonstrated by Scanning Tunneling Microscopy, Phys. Rev. X **5**, 041018 (2015).

[45] T. Kondo, Y. Hamaya, A. D. Palczewski, T. Takeuchi, J. S. Wen, Z. J. Xu, G. Gu, J. Schmalian, and A. Kaminski, Disentangling Cooper-pair formation above the transition temperature from the pseudogap state in the cuprates, Nat. Phys. **7**, 21 (2011).

[46] R. Comin, A. Frano, M. M. Yee, Y. Yoshida, H. Eisaki, E. Schierle, E. Weschke, R. Sutarto, F. He, A. Soumyanarayanan, Y. He, M. Le Tacon, I. S. Elfimov, J. E. Hoffman, G. A. Sawatzky, B. Keimer, and A. Damascelli, Charge order driven by Fermi-Arc instability in $Bi_2Sr_{2-x}La_xCuO_{6+\delta}$, Science **343**, 390 (2014).

[47] S. V. Borisenko, A. A. Kordyuk, A. N. Yaresko, V. B. Zabolotnyy, D. S. Inosov, R. Schuster, B. Büchner, R. Weber, R. Follath, L. Patthey, and H. Berger, Pseudogap and Charge Density Waves in Two Dimensions, Phys. Rev. Lett. **100**, 196402 (2008).

[48] Y. Yang, W.-S. Wang, J.-G. Liu, H. Chen, J.-H. Dai, and Q.-H. Wang, Superconductivity in doped Sr_2IrO_4: A functional renormalization group study, Phys. Rev. B **89**, 094518 (2014).

[49] A. M. Turner and A. Vishwanath, Contemp. Concepts Condens. Matter, Sci.: Topol. Insul. **6**, 293 (2013).